International Journal of Solids and Structures 49 (2012) 1088–1102

Contents lists available at SciVerse ScienceDirect

International Journal of Solids and Structures

journal homepage: www.elsevier.com/locate/ijsolstr

Thermomechanical cyclic behavior modeling of Cu-Al-Be SMA materials and structures

Luc Saint-Sulpice [a,b,c], Shabnam Arbab-Chirani [a,b,c,*], Sylvain Calloch [a,c]

[a] Université Européenne de Bretagne, Laboratoire Brestois de Mécanique et des Systèmes (EA 4325), France
[b] École Nationale d'Ingénieurs de Brest, Technopôle Brest-Iroise, CS 73862, 29238 Brest Cedex 3, France
[c] École Nationale Supérieure des Ingénieurs des Études et Techniques d'Armement, 2 rue François Verny, 29806 Brest Cedex 9, France

ARTICLE INFO

Article history:
Received 3 December 2010
Received in revised form 10 September 2011
Available online 9 February 2012

Keywords:
Shape memory alloys
Cyclic test
Macroscopic modeling
Thermomechanical cyclic loadings
Cu-Al-Be
Jammed martensite
Numerical integration
Finite element analysis
SMA actuators

ABSTRACT

This paper concerns the behavior of Cu-Al-Be polycrystalline shape memory alloys under cyclic thermomechanical loadings. Sometimes, as shown by many experimental observations, a permanent inelastic strain occurs and increases with the number of cycles. A series of cyclic thermomechanical tests has been carried out and the origin of the residual strain has been identified as residual martensite. These observations have been used to develop a 3D macroscopic model for the superelasticity and stress assisted memory effect of SMAs able to describe the evolution of permanent inelastic strain during cycles. The model has been implemented in a finite elements code and used to simulate the behavior of antagonistic actuators based on SMA springs under cyclic thermomechanical loading with a residual displacement appearance.

1. Introduction

The specific thermomechanical behavior of shape memory alloys (SMAs) is due to a solid-to-solid, diffusionless, thermoelastic martensitic phase transformation (e.g., Funakubo, 1987; Otsuka and Wayman, 1999). According to steels, the high and low temperature phases are called austenite and martensite, respectively. The existence of these two phases leads to different types of thermomechanical behaviors making these alloys very specific and attractive.

Among the different thermomechanical behaviors of SMAs, superelasticity (or pseudoelasticity) is particularly interesting. Superelastic behavior is revealed when the material is mechanically stressed above the austenite finish temperature, A_f. The stress–strain response is characterized by a typical hysteretic loop and the material recovers its initial shape after unloading. Sometimes, as shown by many experimental observations (e.g., Šittner et al., 1995; Strnadel et al., 1995a,b; Tanaka et al., 1995; Arrigoni et al., 2001; Gall and Maier, 2002; Krone et al., 2005; Feng and Sun, 2007; Kang et al., 2009; Wang et al., 2010) and as we will see in this paper, the stress–strain superelastic loop is not closed and a residual strain remains after unloading. Another aspect of the thermomechanical behavior is revealed when the material is subjected to a cooling-heating cycle, from an initial temperature above A_f and at a constant stress. The strain-temperature response presents a typical hysteretic loop and the material recovers its initial shape after heating. This is called stress assisted memory effect (SAME). In this case too, in many experimental observations (e.g., Lexcellent et al., 2000; Lahoz and Puértolas, 2004) and as it will be shown in this paper, the strain-temperature loop could not be closed and a residual strain remains at high temperature. These cyclic effects are amplified at high loading rates due to the thermomechanical coupling (e.g., He et al., 2010; He and Sun, 2010).

As it is known, a stable state of the material can be obtained by pre-training. This procedure is at the origin of fatigue effect in SMA by introducing a residual strain which evolves with the cycles. So, it is important to evaluate correctly its evolution with models to improve the reliability of SMA devices and to propose the well adapted fatigue criteria. These criteria should be based on the indicators of the cumulated residual strain.

SMAs superelasticity and stress assisted memory effect have received considerable attention over the last thirty years (e.g., Falk, 1980; Tanaka, 1986; Ball and James, 1987; Patoor et al., 1988; Fischer and Tanaka, 1992; Sun and Hwang, 1993a,b; Raniecki and Lexcellent, 1994; Atanackovic and Müller, 1995; Boyd and

* Corresponding author at: École Nationale d'Ingénieurs de Brest, Technopôle Brest-Iroise, CS 73862, 29238 Brest Cedex 3, France. Tel.: +33 0298056681; fax: +33 0298056653
E-mail addresses: shabnam.arbab@enib.fr, arbab@enib.fr (S. Arbab-Chirani).

0020-7683/$ - see front matter © 2012 Elsevier Ltd. All rights reserved.
doi:10.1016/j.ijsolstr.2012.01.017

Lagoudas, 1996; Lu and Weng, 1997; Arrigoni et al., 2001; Gall and Maier, 2002; McNaney et al., 2003; Bouvet et al., 2004; Nemat-Nasser et al., 2005; Panico and Brinson, 2007; Araya et al., 2008; Wang et al., 2010). Among the great number of investigations, very few studies concern the thermomechanical behavior modeling under cyclic loading. Recently, few models taking into account the residual strain evolution in superelasticity and sometimes for thermomechanical loadings have been proposed in the literature (e.g., Kan and Kang, 2010; Saleeb et al., 2010). In most cases, an internal variable representing permanent inelastic strain is introduced in addition to the transformation and elastic strains. This internal variable is generally related to the classic plastic strain used in plasticity frameworks (Zaki et al., 2010).

This study concerns the thermomechanical behavior (i.e., superelasticity and stress assisted memory effect) of SMAs under cyclic loadings at low strain rates. A particular attention is paid to study and to describe the evolution of the residual strain with the number of cycles.

A three-dimensional macroscopic model able to describe quantitatively superelastic and stress assisted memory effect behaviors under cyclic loadings is proposed. This new model is an extension of the Saint-Sulpice et al. (2009) superelastic model. A certain number of ingredients of the previous version of the model is conserved. For example, the original concept of two different transformation surfaces (i.e., one for forward transformation, and the other one for the reverse transformation) and the relation between the martensite volume fraction and a scalar equivalent transformation strain are re-used. In this new version of the model, a new concept of jammed martensite is introduced. This allows one to describe the stress assisted memory effect under cyclic loadings (it was not the case with the previous model dedicated to superelasticity).

The present paper is organized in five main sections. In the first one, an experimental database is presented concerning the thermomechanical behavior of a Cu-Al-Be SMA under mechanical and thermal cyclic loadings. In the second section, the constitutive equations of the three-dimensional macroscopic model are described in detail. In the third section, the material parameters introduced in the thermomechanical model are identified and comparisons between experimental results and simulations are shown. In the fourth section, the model is implemented in a finite elements code and the numerical integration algorithm is described. In the last section, the cyclic thermomechanical behavior of two SMA actuators have been simulated in a finite elements code using the developed model.

2. Thermomechanical behavior of a Cu-Al-Be SMA under cyclic loadings

A series of tests has been performed to characterize the thermomechanical behavior of the studied material. A particular attention has been paid to the influence of mechanical (isothermal) or thermal cyclic loadings.

2.1. Material and test conditions

The material used for all the tests is a Cu-Al-Be polycrystalline SMA (Cu: 87% at; Al: 11% at; Be: 2% at) provided by Nimesis (France).This shape memory material is available as 0.8 mm diameter wires. The four characteristic transformation temperatures were determined using electric resistivity measurements. Fig. 1 shows the evolution of the resistivity during a cooling-heating cycle. The temperatures M_s^0, M_f^0, A_s^0 and A_f^0 are given in Table 1.

All the tests have been performed on a Zwick electromechanical universal testing machine equipped with a thermal chamber

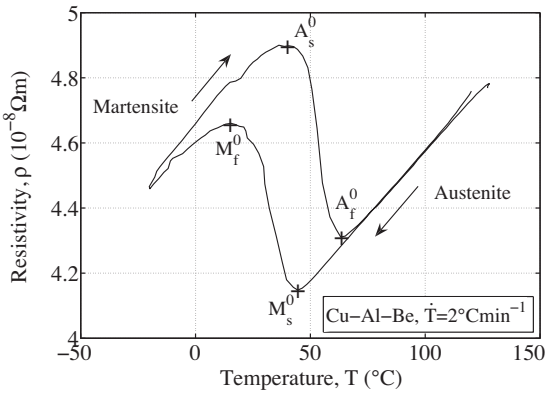

Fig. 1. Evolution of the resistivity versus temperature during a temperature cycle with no stress on a wire of the studied Cu-Al-Be.

Table 1
Characteristic transformation temperatures of the studied Cu-Al-Be.

M_s^0	M_f^0	A_s^0	A_f^0
43 °C	19 °C	40 °C	63 °C

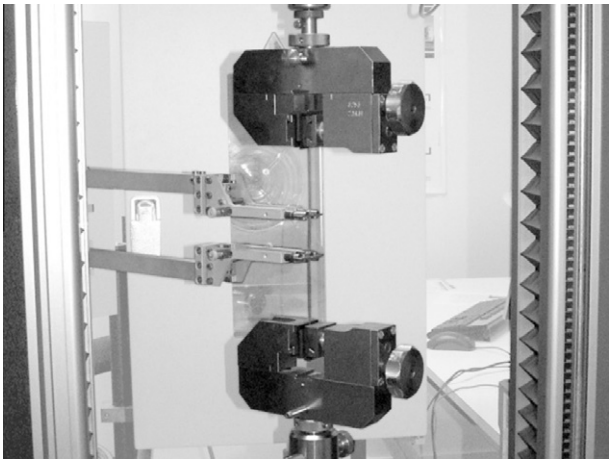

Fig. 2. Experimental setup used for tensile tests.

(with a temperature range of − 80 °C–200 °C) (Fig. 2). A 25 mm extensometer has been used to measure the axial strain. Stress has been determined using the load cell of the testing machine, with 500 N range. Temperature has been measured by a K type thermocouple. The isothermal superelastic tests have been performed under axial strain control. A low strain rate (i.e., $\dot{\varepsilon} = 10^{-4}\ s^{-1}$) has been chosen to minimize temperature rise due to self-heating of the material. During non-isothermal testing (i.e., stress assisted memory effect tests), a temperature rate of ± 2.5 °C.min^{-1} has been chosen during the heating and cooling phases, respectively.

2.2. Tensile loading–unloading test and stress assisted memory effect test

First, the superelastic behavior under tensile loading–unloading of the material has been studied. A specimen has been deformed up to a maximum strain of 4% at 80 °C and then unloaded down to zero stress. Fig. 3a shows the corresponding typical hysteretic superelastic strain–stress curve. After the initial elastic behavior,

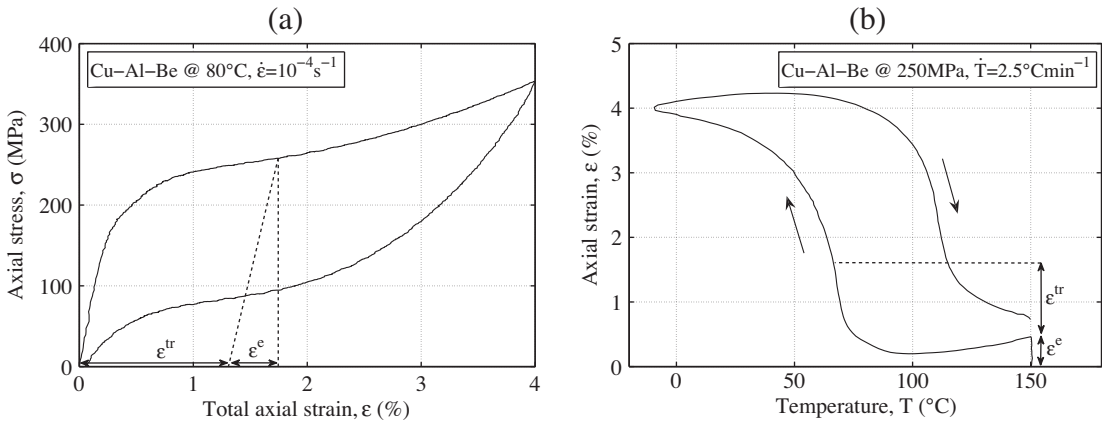

Fig. 3. Evolution of (a) stress versus strain during a tensile test and (b) strain versus temperature during a thermal cycle under constant stress.

a supplementary deformation, ε^{tr}, occurs via the martensitic phase transformation. In the case of the studied material, a little residual strain remains after unloading.

The stress assisted memory effect has been studied on a second specimen. The thermomechanical loading considered here has two different sequences. The first one consists in applying a loading up to a stress level of 250 MPa at a temperature higher than A_f (i.e., 150 °C). A cooling-heating cycle under a constant stress level of 250 MPa is then performed in the second sequence of the test. Fig. 3b shows the corresponding typical hysteretic temperature-strain curve. As long as the temperature is higher than $M_s^{\sigma=250\ \mathrm{MPa}}$, the strain evolves just by thermal effect. When the temperature is lower than $M_s^{\sigma=250\ \mathrm{MPa}}$, the martensitic phase transformation takes place and the strain increases significantly until the temperature is lower than $M_f^{\sigma=250\ \mathrm{MPa}}$. Then the sample is in a fully stress-induced martensitic state and the strain evolves again just by thermal effect. During the heating phase, as long as the temperature is lower than $A_s^{\sigma=250\ \mathrm{MPa}}$, the strain evolves just by thermal effect. When the temperature is higher than $A_s^{\sigma=250\ \mathrm{MPa}}$, reverse phase transformation takes place and the strain decreases significantly until the temperature is higher than $A_f^{\sigma=250\ \mathrm{MPa}}$. Here again, it can be observed that a little residual strain remains after the heating phase (i.e., at the end of the cycle).

2.3. Return memory point effect under mechanical and thermomechanical loadings

The return point memory effect (RPME) is a very special aspect of the thermomechanical behavior of shape memory alloys. This effect was formulated by Ortin (1992) and is very similar to the "discrete memory" notion of Guélin (1980). This effect can be observed as well in superelastic behavior as in stress assisted memory effect. The RPME concept is based on a set of memory points (MP), which are local extrema of the stress–strain curve. Fig. 4a and b show the strain loading path and the corresponding strain–stress curve in the case of superelastic behavior. The specimen has been loaded up to 4% strain level (A), then unloaded down to 2% (B), then reloaded up to 3% (C), and re-unloaded down to 1% (D), then reloaded up to 4% (E) and finally unloaded down to zero stress (F). Along the path (OA), there is no MP because the material is virgin. After the first inversion in the loading direction, point A becomes a maximum memory point and is "memorized" by the material. At point B, the loading direction is reversed once again. Point B becomes a minimum memory point. After the new inversion of the loading direction at C, C becomes a maximum memory point. Subsequently, it can be observed, on the one hand, that the path (CD) passes by the minimum memory point B. On the other hand, because the internal loop (CB) is closed, the maximum memory point (C) is "forgotten" and the path (DE) passes by the maximum memory point (A) (i.e., A = E). The internal loop (ED) is then closed, the minimum memory point (D) is "forgotten". So, the last unloading (AF) does not go through point (D).

The illustration of the concept of return memory point during a stress assisted memory effect test including an internal loop is shown on Fig. 5a and b. It can be observed that the path (CD) passes by the maximum memory point (B) and because the internal loop (BC) is closed the minimum memory point (C) is "forgotten". So, the last heating phase (DE) does not go through point (C).

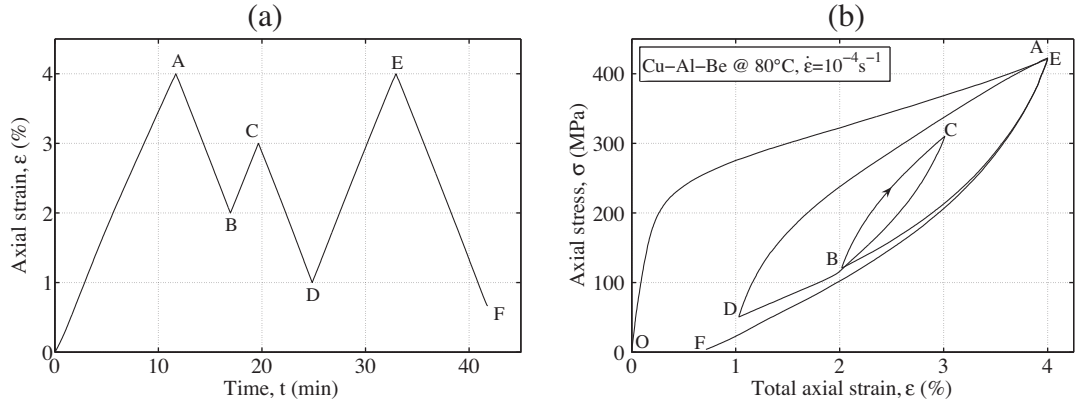

Fig. 4. (a) Stress loading path and (b) evolution of stress versus strain during a tensile test with return point memory effect.

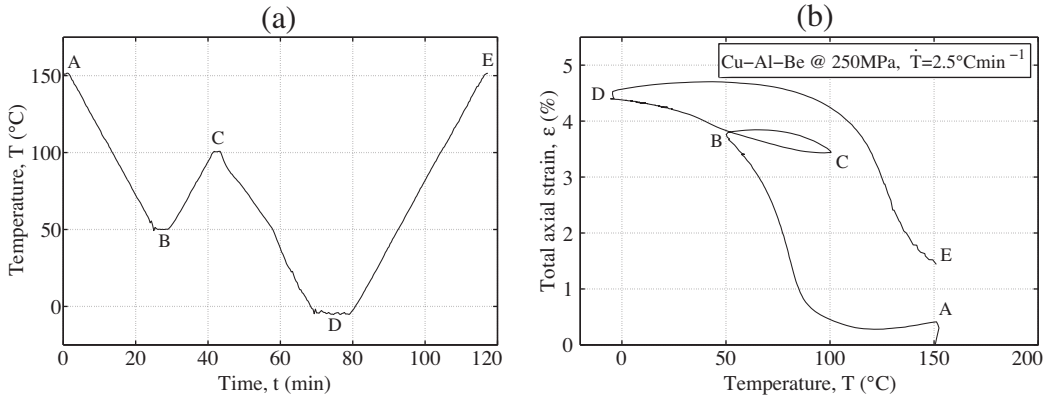

Fig. 5. (a) Temperature loading path and (b) evolution of strain versus temperature during a thermal cycle under constant stress.

We will see, in the section concerning the thermomechanical modelization, how this particular aspect of the thermomechanical behavior of shape memory alloys is taken into account.

2.4. Superelastic and SAME under cyclic loading at constant amplitude

Two additional tests under cyclic loading at constant amplitude have been performed. The main objective of these tests is to study the evolution of the residual strain with the number of cycles.

First, a series of four tests at 80 °C has been performed concerning the superelastic behavior of the material. Fig. 6a shows the corresponding strain–stress response for a strain amplitude of 4%. The residual strain increases with the number of cycles up to a saturated value. Fig. 6b shows the evolution of the residual strain versus the number of cycles for four different strain amplitudes (i.e., 1, 2, 3 and 4%). It can be observed that the saturated value depends on the strain amplitude: the higher is the strain amplitude, the greater is the obtained saturated residual strain.

A cyclic stress assisted memory effect test has been performed between 150 °C and − 10 °C. Fig. 7a shows the corresponding temperature-strain response. It can be observed, on the one hand, that the residual strain at high temperature (i.e., 150 °C) increases with

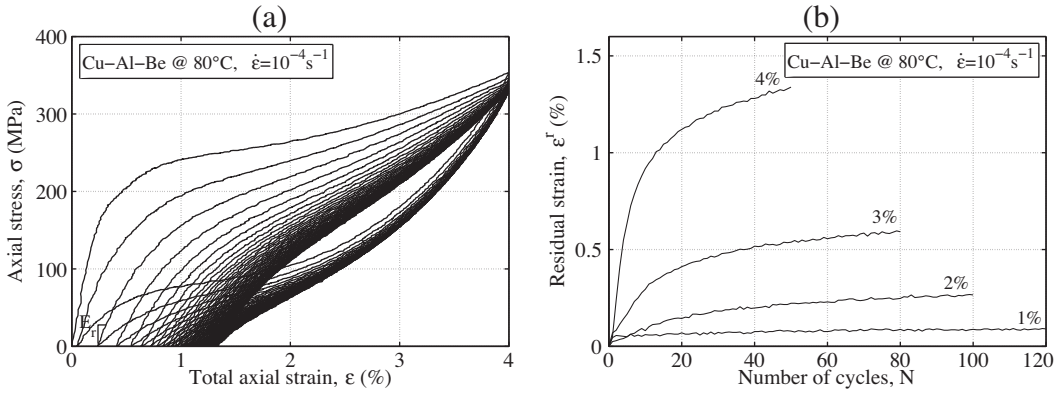

Fig. 6. Evolution of (a) stress versus strain during a cyclic tensile test at 4% strain amplitude and (b) residual strain versus number of cycles during cyclic tensile tests at 1, 2, 3 and 4% strain amplitude.

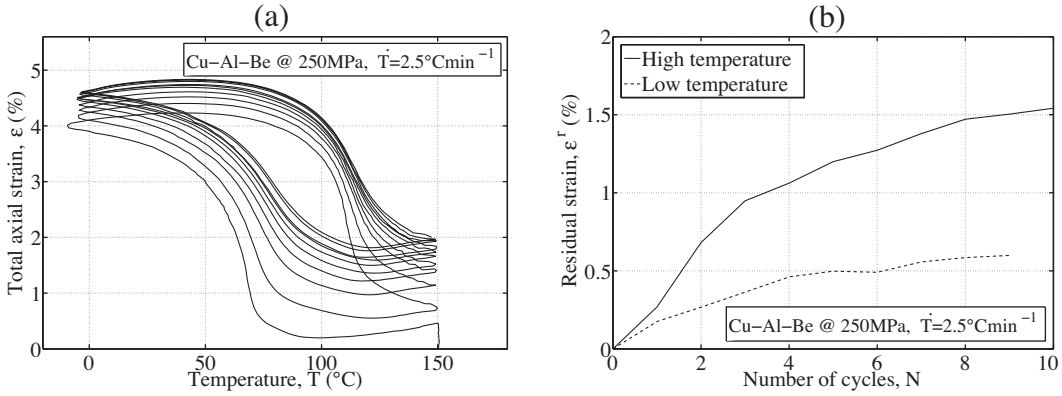

Fig. 7. Evolution of (a) strain versus temperature and (b) residual strain versus number of cycles during a thermal cyclic loading under constant stress.

the number of cycles. On the other hand, the maximum strain at low temperature (i.e., −10 °C) increases too. Fig. 7b shows the evolution of the residual strain at high temperature and the maximum strain at low temperature with the number of cycles.

2.5. Superelastic behavior under variable-amplitude cyclic loading

Two additional superelastic tests have been performed to study the evolution of residual strain under variable-amplitude cyclic loading. The first test is based on two sequences. In each sequence, the sample is subjected to a loading–unloading cycle up to 4% strain level followed by fifty cycles at 2%. Fig. 8a and b show the corresponding strain–stress response and the evolution of the residual strain with the number of cycles. It can be observed that the residual strain increases quickly during the first cycle of each sequence (i.e., the cycle at 4% amplitude) and more slowly during the cycles at 2%. The evolution of the residual strain versus the number of cycles can be compared to those obtained under cyclic loading at constant amplitude (i.e., 2 and 4%).

The second test is an increasing amplitude one. During each cycle, the sample is subjected to a loading–unloading up to 0.5% strain higher than the previous cycle one. Fig. 9a and b show the

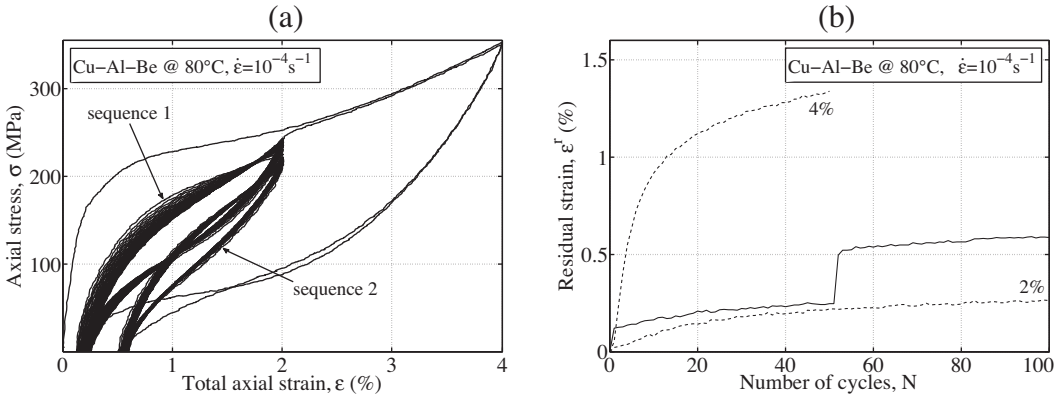

Fig. 8. Evolution of (a) stress versus strain and (b) residual strain versus number of cycles during a cyclic tensile test with variable amplitude.

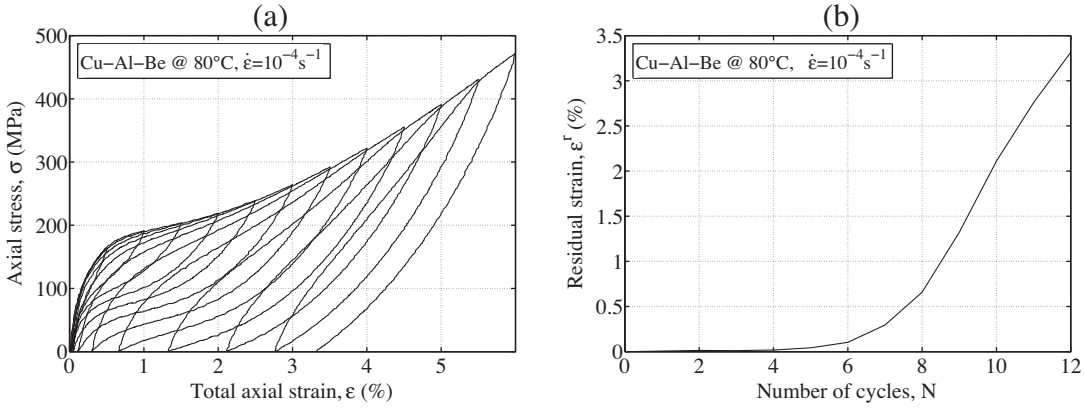

Fig. 9. Evolution of (a) stress versus strain and (b) residual strain versus number of cycles during a cyclic tensile test with increasing amplitude.

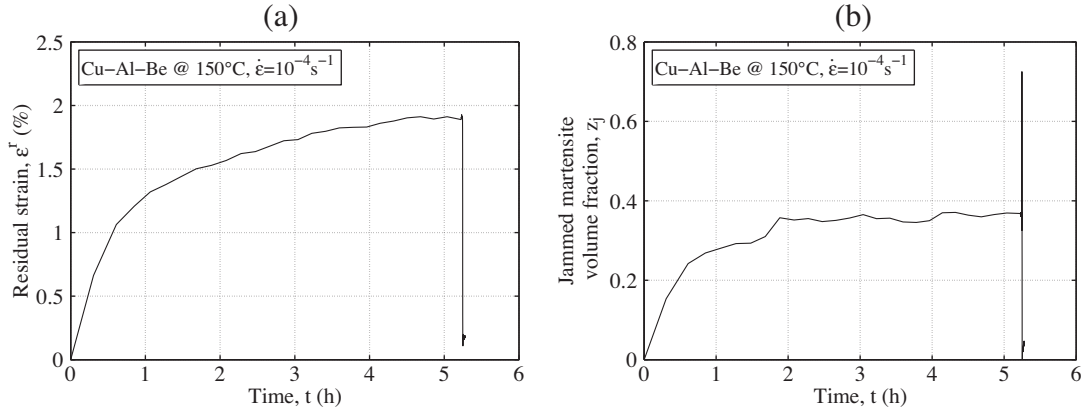

Fig. 10. Evolution of (a) the residual strain and (b) martensite volume fraction versus time during a cyclic tensile test followed by a thermal flash.

corresponding strain–stress response and the evolution of the residual strain with the number of cycles. It can be observed that, for this test, the residual strain increases without saturating unlike the previous cyclic tests.

2.6. Thermal flash test

This last test has been performed to determine the origin of the residual strain observed in the previous tests. The concept of "thermal flash test" has been already introduced in Saint-Sulpice et al. (2009). This specific test was performed after a superelastic cyclic loading at constant amplitude (e.g., 4% amplitude). It consists in heating the specimen at approximately 150 °C higher than the test temperature for a few seconds and observing the evolution of the residual strain. Fig. 10a and b show the evolution of the residual strain during the cyclic test and during the "thermal flash test". It can be observed the disappearance of 90% of the residual strain. This experimental result confirms that, for our Cu-Al-Be SMA, the main origin of the residual strain under cyclic loadings is due to the jammed martensite. In these alloys the existence of precipitates blocks the reverse transformation of martensite to austenite. Indeed, if the origin of the residual strain was plasticity, the duration and the reached low level of the temperature of the thermal flash test does not allow the restoration process of classic plastic strain.

3. Macroscopic 3D modeling of SMA behavior

The proposed model is the extension of the one developed in Saint-Sulpice et al. (2009) which allows us to simulate the cyclic superelasticity behavior of SMA under general multiaxial nonproportional loading. The main originality of this previous model concerns the description of the elastic domain of the material by two different transformation surfaces for forward and reverse transformation noted f_1 and f_2, respectively (Fig. 11).

Over and above the other particularities of the behavior, the definition of these two transformation surfaces allows us to describe the reverse transformation for every SMA (Copper-based, Ni-Ti, ...) and in particularly the reorientation of martensite observed under nonproportional loadings. The previous model allows us to take into account the residual strain that appears under cyclic mechanical loadings. The evolution of this residual strain is based on a particular transformation kinetics driven by a cumulated transformation strain, *tr*.

In this work, modifications are proposed to take into account the evolution of the residual strain during thermomechanical loadings. The cumulated transformation strain, *tr*, controls the appearance of residual martensite which leads to the evolution of the residual strain under cyclic loadings. This allows us to reproduce the 3D super-elasticity and also the stress assisted memory effect under cyclic loadings.

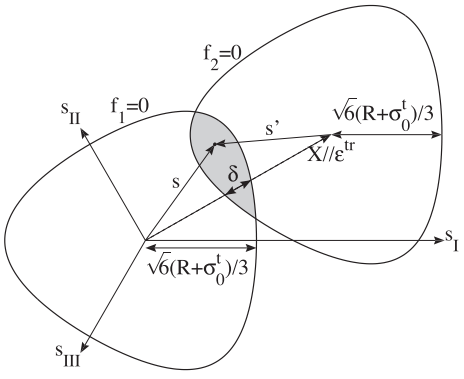

Fig. 11. Forward and reverse transformation surfaces.

In the following sections, the constitutive equations of the model are detailed.

3.1. Strain decomposition and relation with the volume fraction of martensite

The framework of small strains has been assumed. So, the classic decomposition of the total strain, $\boldsymbol{\varepsilon}$, without plasticity, is considered:

$$\boldsymbol{\varepsilon} = \boldsymbol{\varepsilon}^e + \boldsymbol{\varepsilon}^{tr} = \boldsymbol{E}^{-1}\ \boldsymbol{\sigma} + \boldsymbol{\varepsilon}^{tr} \tag{1}$$

where $\boldsymbol{\varepsilon}^e$ and $\boldsymbol{\varepsilon}^{tr}$ are the elastic and transformation strain tensors, respectively (Fig. 3a) and $\boldsymbol{\sigma}$ the stress tensor. In order to simplify the problem, the same elastic characteristic, $\boldsymbol{E}$, is assumed for austenitic and martensitic phases.

The martensite volume fraction, z, is defined by a relation initially proposed by Vacher and Lexcellent (1991) and experimentally validated by Gedouin et al. (2010) and by Taillard et al. (2008) for multiaxial loadings:

$$z = \frac{\varepsilon_{eq}^{tr}}{\gamma} \tag{2}$$

where γ is a material parameter corresponding to the maximum equivalent transformation strain. The equivalent transformation strain, ε_{eq}^{tr}, is defined by Bouvet et al. (2004):

$$\varepsilon_{eq}^{tr} = \sqrt{\frac{\boldsymbol{\varepsilon}^{tr} : \boldsymbol{\varepsilon}^{tr}}{\boldsymbol{K}_\sigma : \boldsymbol{K}_\sigma}} \approx \overline{\varepsilon^{tr}} \frac{g(-y_\varepsilon)}{g(-1)} \tag{3}$$

where $\boldsymbol{K}_\sigma$ is the tensor normal to the forward transformation surface, given by:

$$\boldsymbol{K}_\sigma = \frac{\partial \sigma_{eq}}{\partial \boldsymbol{\sigma}} = \frac{3}{2} g(y_\sigma) \left(3\boldsymbol{N}_\sigma^2 - y_\sigma \boldsymbol{N}_\sigma - \frac{2}{3}\boldsymbol{I}_d \right) \tag{4}$$

With $\boldsymbol{N}_\sigma = \frac{\boldsymbol{s}}{\bar{\sigma}}$, $y_\varepsilon = 4\dfrac{\det(\boldsymbol{\varepsilon}^{tr})}{\bar{\varepsilon}^{tr\,3}}$ is the third strain invariant, $\bar{\varepsilon}^{tr} = \sqrt{\frac{2}{3}\boldsymbol{\varepsilon}^{tr} : \boldsymbol{\varepsilon}^{tr}}$ is the von Mises equivalent strain and $g(y)$, σ_{eq}, $\bar{\sigma}$ and y_σ are described in the next section.

3.2. Description of the forward and reverse transformation surfaces

Two transformation surfaces are used in the model. The first one, f_1, drives the forward transformation, and the second one, f_2, drives the reverse transformation. The forward transformation surface depends on the second and third stress invariants, and is given by the following equation:

$$f_1 = \bar{\sigma} - \frac{R(z) + \sigma_0^t(T)}{g(y_\sigma)} \leqslant 0 \tag{5}$$

where $\bar{\sigma} = \sqrt{\frac{3}{2}\boldsymbol{S} : \boldsymbol{S}}$ is the von Mises equivalent stress with $\boldsymbol{S}$ the deviatoric stress tensor, $g(y) = \cos\left(\dfrac{\arccos(1 - a(1-y))}{3}\right)$ describes the shape of the transformation surface and the tensile-compression asymmetry observed in shape memory alloys (e.g., Vacher and Lexcellent, 1991; Patoor et al., 1995; Gall et al., 1997; Liu et al., 1998; Orgéas and Favier, 1998) with a the from 0 to 1 (Bigoni and Piccolroaz, 2004), $y_\sigma = \dfrac{27}{2}\dfrac{\det(\boldsymbol{S})}{\bar{\sigma}^3}$ is the third stress invariant, $R(z)$ is the size of the transformation surface and $\sigma_0^t(T) = \mu(T - T_0)$ is the transformation stress under tensile loading depending on the temperature, T, with μ and T_0 two material parameters.

The equivalent stress used in following equations depends on the von Mises equivalent stress, $\bar{\sigma}$, and the g function:

$$\sigma_{eq} = \bar{\sigma} g(y_\sigma) \tag{6}$$

The shape and the size of the reverse transformation surface are the same as the first one:

$$f_2 = \overline{\boldsymbol{\sigma} - \boldsymbol{X}} - \frac{R(z) + \sigma_0^t(T)}{g(y_{\sigma-X})} \leqslant 0 \tag{7}$$

With:

$$y_{\sigma-X} = \frac{27}{2} \frac{\det(\boldsymbol{S} - \boldsymbol{X})}{\overline{\boldsymbol{\sigma} - \boldsymbol{X}}^3} \tag{8}$$

where $\boldsymbol{X}$ is the kinematic tensor colinear to $\boldsymbol{\varepsilon}^{tr}$ which determines the position of the center of f_2 and is given by the following equation:

$$\boldsymbol{X} = \left((R(z) + \sigma_0^t(T)) \left(\frac{1}{g(y_\varepsilon)} + \frac{1}{g(-y_\varepsilon)} \right) - \delta(z) \right) \frac{\boldsymbol{\varepsilon}^{tr}}{\sqrt{\frac{3}{2} \boldsymbol{\varepsilon}^{tr} : \boldsymbol{\varepsilon}^{tr}}} \tag{9}$$

where $\delta(z)$ is the size of the intersection of the two transformation surfaces in the $\boldsymbol{\varepsilon}^{tr}$ direction (Fig. 11, grayed zone). It will be detailed in the following section.

3.3. Transformation strain evolution

During transformation, the evolution of the transformation strain, $\boldsymbol{\varepsilon}^{tr}$, respects the following transformation rules. For forward transformation, the normality law is respected so the direction of the transformation strain evolution is normal to the forward transformation surface (Fig. 12a).

This has been experimentally validated under biaxial tension–compression loadings by Bouvet et al. (2002) and under tension–torsion loadings by Taillard (2006). However during reverse transformation a non-associated frame is defined. The direction of the transformation strain evolution is the same as the direction of the transformation strain (Fig. 12b).

$$\begin{cases} \dot{\boldsymbol{\varepsilon}}^{tr} = \dot{\lambda}_1 \frac{\partial f_1}{\partial \boldsymbol{\sigma}} = \frac{\gamma \dot{z}}{\boldsymbol{K}_\varepsilon : \boldsymbol{K}_\sigma} \boldsymbol{K}_\sigma & (\dot{z} > 0) \\ \dot{\boldsymbol{\varepsilon}}^{tr} = -\dot{\lambda}_2 \frac{\boldsymbol{\varepsilon}^{tr}}{\bar{\varepsilon}^{tr}} = \gamma \dot{z} \frac{g(-1)}{g(-y_\varepsilon)} \frac{\boldsymbol{\varepsilon}^{tr}}{\bar{\varepsilon}^{tr}} & (\dot{z} < 0) \end{cases} \tag{10}$$

where $\dot{\lambda}_1$ and $\dot{\lambda}_2$ are the transformation multipliers given by the consistency conditions, and $\boldsymbol{K}_\varepsilon$ is the tensor normal to the forward transformation surface in the strain space, given by:

$$\boldsymbol{K}_\varepsilon = \frac{\partial \varepsilon_{eq}^{tr}}{\partial \boldsymbol{\varepsilon}^{tr}} = \frac{1}{g(-1)} \left(\frac{2}{3} g(-y_\varepsilon) \boldsymbol{N}_\varepsilon + 2 g'(-y_\varepsilon) \left(-2 \boldsymbol{N}_\varepsilon^2 + y_\varepsilon \boldsymbol{N}_\varepsilon + \boldsymbol{I}_d \right) \right) \tag{11}$$

With $\boldsymbol{N}_\varepsilon = \frac{\boldsymbol{\varepsilon}^{tr}}{\bar{\varepsilon}^{tr}}$.

A special case occurs during non-proportional loadings when both transformation surfaces are reached at the same time (Fig. 13). When this happens, forward and reverse transformations occur simultaneously leading to the evolution of the transformation strain direction with an almost constant volume fraction of martensite.

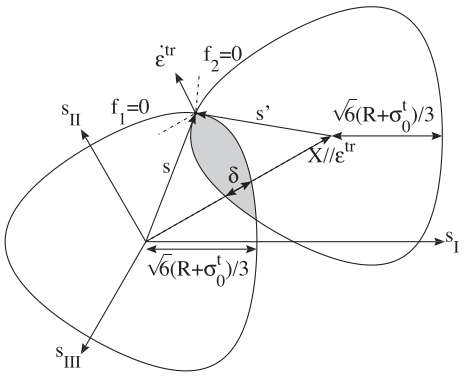

Fig. 13. Forward and reverse transformation surfaces and transformation strain evolution during reorientation.

In this case, the evolution of the transformation strain is a combination of those during forward and reverse transformation. Its direction is determined directly by the numerical integration process (see Section 5). Nevertheless the evolution of the equivalent transformation strain is given by:

$$\dot{\varepsilon}_{eq}^{tr} = \dot{\lambda}_1 \boldsymbol{K}_\varepsilon : \boldsymbol{K}_\sigma + \dot{\lambda}_2 \frac{g(-y_\varepsilon)}{g(-1)} \tag{12}$$

3.4. Transformation surfaces evolution

During transformation, the shape memory alloy behavior is described by the evolution of the two variables $R(z)$ and $\delta(z)$ which respectively lead the size and the position of the two transformation surfaces. In order to take into account the return point memory effect described on Fig. 4b and Fig. 5b, the volume fraction of martensite is memorized at each change of the loading way: z_n^{max} for a high memory point and z_n^{min} for a low memory point, where n is the number of opened loops of loading. Then, the evolution of the two variables, $R(z)$ and $\delta(z)$, depends on the memorized volume fraction of martensite. During forward transformation the evolution of $\delta(z)$ is given by:

$$\delta(z) = \delta_0 + \left(p \frac{z - z_{n-1}^{min}}{z_{n-1}^{max} - z_{n-1}^{min}} - p \right) \left(\delta_{n-1}^{min} - \delta_0 \right) + \left(p \frac{z_{n-1}^{max} - z}{z_{n-1}^{max} - z_{n-1}^{min}} - p \right) \left(\delta_{n-1}^{max} - \delta_0 \right) \tag{13}$$

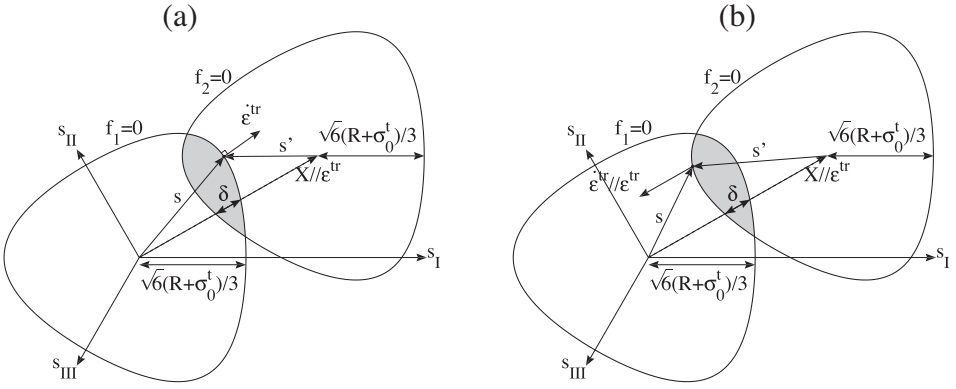

Fig. 12. Forward and reverse transformation surfaces and evolution of the transformation strain during (a) forward transformation and (b) reverse transformation.

During reverse transformation:

$$\delta(z) = \delta_0 + \left(p\frac{z - z_{n-1}^{min}}{z_n^{max} - z_{n-1}^{min}} - p\right)\left(\delta_{n-1}^{min} - \delta_0\right) + \left(p\frac{z_n^{max} - z}{z_n^{max} - z_{n-1}^{min}} - p\right)\left(\delta_n^{max} - \delta_0\right) \quad (14)$$

where $\delta_n^{min} = \delta(z_n^{min})$, $\delta_n^{max} = \delta(z_n^{max})$, p and δ_0 are two material parameters. In the first loop, $\delta(z)$ varies from an initial value δ_1^{min} to the same final value by taking an intermediate value δ_0. δ_1^{min} corresponds to the temperature difference between forward transformation beginning and reverse transformation ending up to a μ factor (Fig. 14a).

During an internal loop, $\delta(z)$ varies from the value of δ at the last high or low memory point to its value at the last low or high memory point (Fig. 14b).

The evolution of $R(z)$ is given during forward transformation by:

$$R(z) = R_{n-1}^{min} + h_1(z)\left(R_{n-1}^{max} - R_{n-1}^{min}\right) \quad (15)$$

During reverse transformation by:

$$R(z) = R_{n-1}^{min} - \delta_{n-1}^{min} + h_2(z)\left(R_n^{max} - \delta_n^{max} - R_{n-1}^{min} + \delta_{n-1}^{min}\right) \quad (16)$$

where $R_n^{min} = R(z_n^{min})$ and $R_n^{max} = R(z_n^{max})$. Then, during the first loop, $R(z)$ varies between $R_1^{min} = 0$ and R_1^{max}, which is a material parameter (Fig. 15a). During an internal loop, it varies between the values of R at the last low and high memory points (Fig. 15b).

The evolution of $R(z)$ between these values is given by the functions $h_1(z)$ and $h_2(z)$ for forward and reverse transformation respectively:

$$h_1(z) = \frac{h\left(\frac{z_{n-1}^{max}}{z_1^{max}}\frac{z - z_{n-1}^{min}}{z_{n-1}^{max} - z_{n-1}^{min}}\right)}{h\left(\frac{z_{n-1}^{max}}{z_1^{max}}\right)} \quad (17)$$

$$h_2(z) = \frac{h\left(\frac{z(z_1^{max} - z_{n-1}^{min}) + z_{n-1}^{min}(z_n^{max} - z_1^{max})}{z_1^{max}(z_n^{max} - z_{n-1}^{min})}\right) - h\left(\frac{z_{n-1}^{min}}{z_1^{max}}\right)}{1 - h\left(\frac{z_{n-1}^{min}}{z_1^{max}}\right)} \quad (18)$$

With:

$$h(z) = \frac{\arccos(1 - 2z)}{\pi} \quad (19)$$

3.5. Cyclic behavior

The cyclic behavior under loadings with constant amplitudes is firstly described. Then, modifications are introduced in order to take into account the effect of amplitude variations during loadings.

3.5.1. Under loadings with constant amplitudes

As it has been observed during experiments (see Section 2.6), a jammed martensite volume fraction, z_j, is introduced in the model in order to take into account the residual strain evolution during

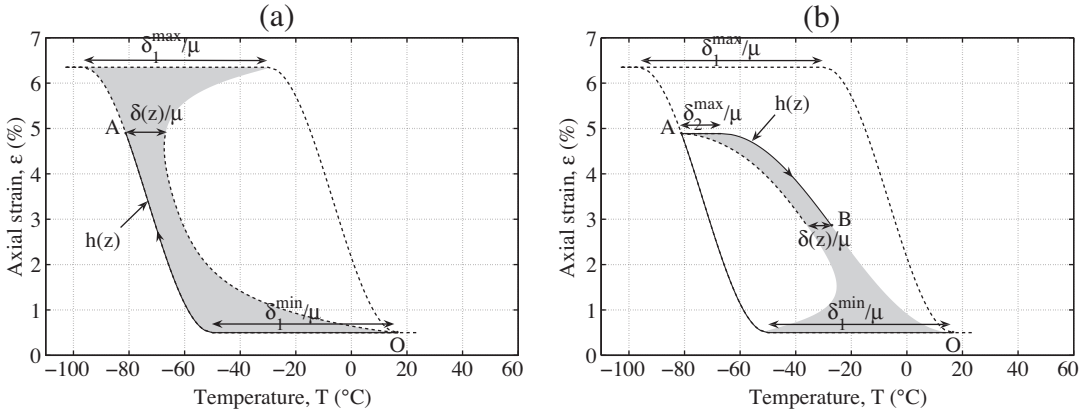

Fig. 14. Evolution of $\delta(z)$ during a thermal loading: (a) cooling and (b) heating.

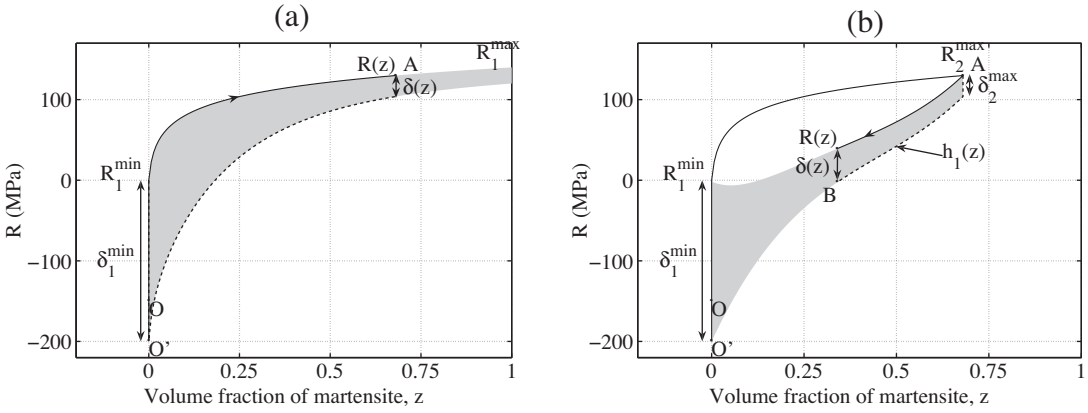

Fig. 15. Evolution of $R(z)$ during a tensile loading: (a) loading and (b) unloading.

Table 2
Material parameters for the studied Cu-Al-Be at room temperature.

E	ν	γ	a	μ
43 GPa	0.3	5.85%	0.7	3 MPa°C^{-1}

T_0	δ_1^{min}	δ_0	R_1^{max}	A	B	C	tr_0
28.7 °C	185 MPa	15 MPa	330 MPa	0.0057	7.05	0.904	0.123

cyclic loadings. This volume fraction is a part of the total martensite volume fraction, z. It increases during forward transformation but does not disappear and remains constant during reverse transformation. Its evolution is given by:

$$\begin{cases} \dot{z}_j = \frac{AB^{\Delta z}}{tr+tr_0}\dot{tr} & (\dot{z} > 0) \\ \dot{z}_j = 0 & (\dot{z} < 0) \end{cases} \tag{20}$$

where A, B and tr_0 are three material parameters, Δz is the loading amplitude of transformation:

$$\Delta z = z - z_{n-1}^{min} \tag{21}$$

and tr is the cumulated transformation strain defined by:

$$tr = \int \left| \frac{\mathrm{d}\varepsilon_{eq}^{tr}}{\gamma} \right| \tag{22}$$

where $\mathrm{d}\varepsilon_{eq}^{tr}$ is the increment of the equivalent transformation strain.

3.5.2. Under loadings with variable amplitudes

In order to take into account the variation of amplitude, first the value of the jammed martensite volume fraction which would be reached during a cyclic test at constant amplitude (using the integrated form of the Eq. (20)) is introduced:

$$z_{jca} = AB^{\Delta z}\ln(tr + tr_0) - A\ln(tr_0) \tag{23}$$

Then the evolution of the jammed martensite volume fraction is given by Eq. (24) using the value of z_{jca}:

$$\dot{z}_j = \frac{AB^{\Delta z}\mathrm{e}^{\frac{z_{jca}-z_j}{C}}}{tr + tr_0}\dot{tr} \tag{24}$$

where C is a material parameter.

4. Identification and validation

The proposed model includes 13 material parameters. Five experimental tests have been used to identify all these parameters, and three different experimental tests have been used to validate the model's behavior. The identified material parameters are given in Table 2.

They have been determined from the cyclic tensile tests at 1, 2, 3 and 4% strain amplitudes (see Fig. 6), and the cyclic tensile test with variable amplitude (see Fig. 8). Fig. 16a, Fig. 17a, Fig. 16b and Fig. 17b show the results of the identification of the behavior for the first two figures and of the residual strain for the two others.

The model's behavior has been then validated by comparing the results of other cyclic tests with the results of corresponding simulations. Fig. 18a shows the result of the simulation of a cyclic tensile test with increasing amplitude (0.5, 1, 1.5, 2, …, 6%). Fig. 18b compares the evolution of the residual strain versus cumulated transformation strain for the experimental test and the corresponding simulation.

Fig. 19a shows the validity of the model during a cyclic assisted two-way memory effect. Fig. 19b compares the evolution of the residual strain at low and high temperatures for the cyclic experimental test and the corresponding simulation. One can observe on Fig. 19a and b that a residual strain is present at low temperature. This residual strain is probably due to a plastic strain of the martensite phase. In the present version of the model, plastic deformation is not taken into account. This explains the difference between the experimental and numerical results at low temperatures.

5. Numerical integration

After the validation of the model, in order to use it in a finite elements code, its numerical integration should be considered.

The global numerical algorithm of the model is described on Fig. 20. It consists to follow this procedure for each step:

1. the elastic prediction of the stress, $\boldsymbol{\sigma}$, is calculated from the initial stress $\boldsymbol{\sigma}_n$ and the strain increment, $\Delta\boldsymbol{\varepsilon}$, imposed by the finite element code,
$$\boldsymbol{\sigma} = \boldsymbol{\sigma}_n + \boldsymbol{E}\Delta\boldsymbol{\varepsilon} \tag{25}$$
2. the forward and reverse transformation functions, f_1 and f_2, are evaluated from the predicted stress, $\boldsymbol{\sigma}$ (Eqs. (5) and (7)),
3. from the calculated values of f_1 and f_2, four cases are possible:
   (a) ($f_1 < 0$ or ($f_1 = 0$ and $\dot{f}_1 < 0$)) and ($f_2 < 0$ or ($f_2 = 0$ and $\dot{f}_2 < 0$)): the elasticity assumption is validated and the calculated stress is used as the initial stress for the next step.
   (b) ($f_1 = 0$ and $\dot{f}_1 = 0$) and ($f_2 < 0$ or ($f_2 = 0$ and $\dot{f}_2 < 0$)): the forward transformation takes place and a correction must be realized on the elastic calculated stress, $\boldsymbol{\sigma}$.

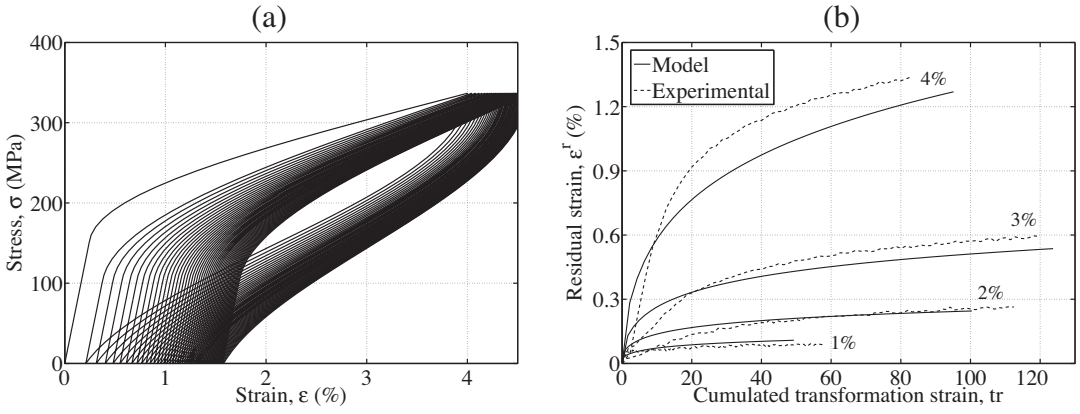

Fig. 16. Evolution of (a) stress versus strain during the simulation of a cyclic tensile test at 4% strain amplitude and (b) residual strain versus cumulated transformation strain during the simulation of cyclic tensile tests at 1, 2, 3 and 4% strain amplitude used for identification with the experimental results.

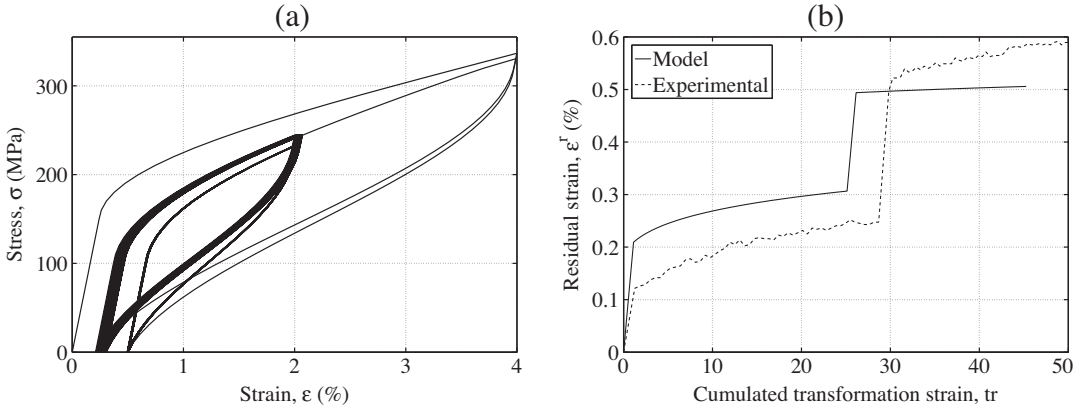

Fig. 17. Evolution of (a) stress versus strain and (b) residual strain versus cumulated transformation strain during the simulation of a cyclic tensile test with variable amplitude used for identification with the experimental results.

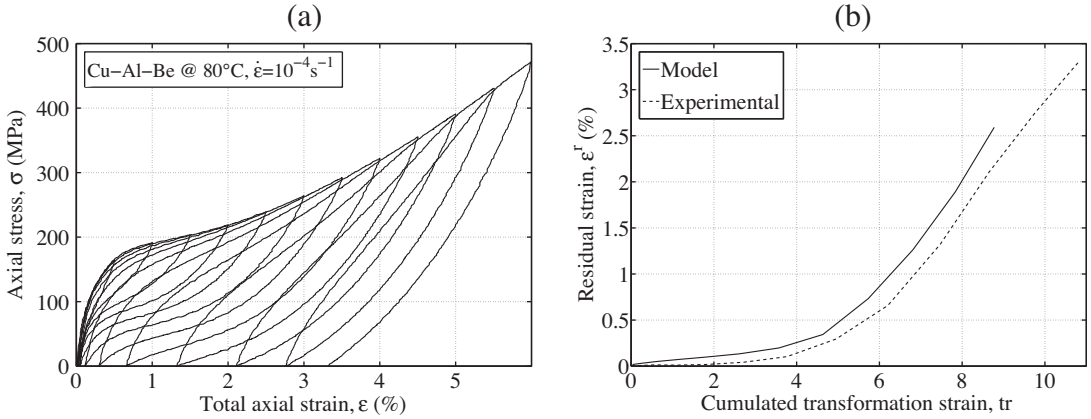

Fig. 18. Evolution of (a) stress versus strain and (b) residual strain versus cumulated transformation strain during the simulation of a cyclic tensile test with increasing amplitude used for validation with the experimental results.

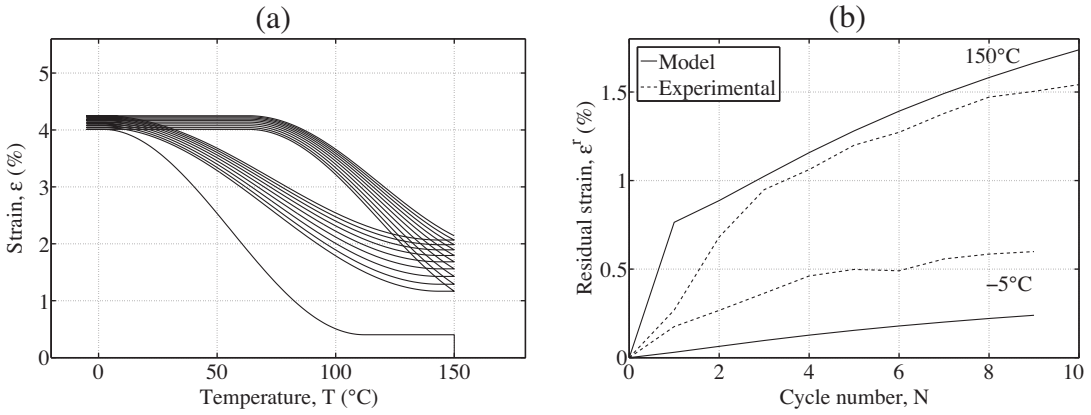

Fig. 19. Evolution of (a) strain versus temperature and (b) residual strain versus cycles during the simulation of a thermal cyclic loading under constant stress used for validation with the experimental results.

(c) ($f_1 < 0$ or ($f_1 = 0$ and $\dot{f}_1 < 0$)) and ($f_2 = 0$ and $\dot{f}_2 = 0$): the reverse transformation takes place and in this case a correction must also be realized on the elastic calculated stress.
(d) ($f_1 = 0$ and $\dot{f}_1 = 0$) and ($f_2 = 0$ and $\dot{f}_2 = 0$): the reorientation takes place.

As described on the Fig. 21, the reorientation is realised by alternating between forward and reverse transformation. The final stress state is reached when both transformation functions value are lower than a precision, p. This alternance leads to the evolution of the transformation strain direction without a significant variation of the martensite volume fraction (see Fig. 22).

During forward transformation the correction of the elastic predicted stress is calculated with the method introduced by Ortiz and Simo (1986): the return-mapping integration algorithm. It consists in the determination of the needed increment of the martensite

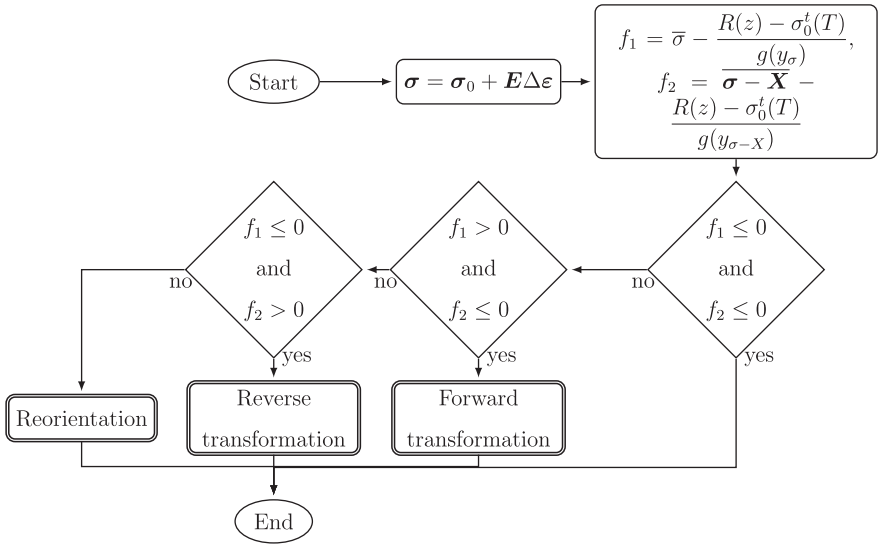

Fig. 20. Global flowchart of the numerical integration method used in the model.

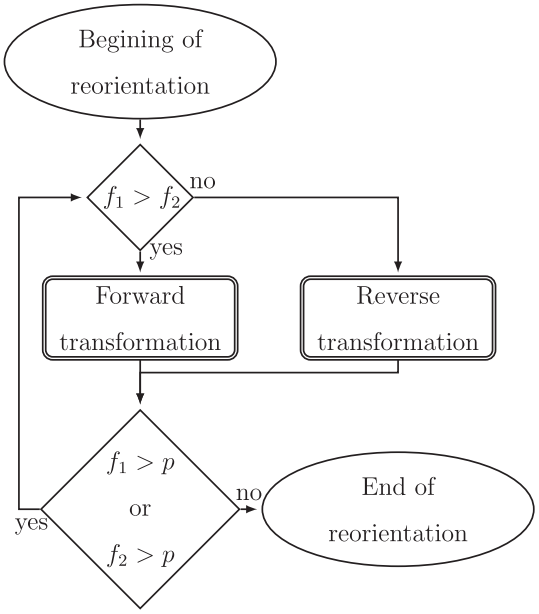

Fig. 21. Flowchart of the numerical integration of the reorientation.

volume fraction, dz, with a Taylor expansion of the transformation function for a stress, $\boldsymbol{\sigma}$, at iteration, $j+1$:

$$f_1^{j+1} = f_1^j + \frac{\partial f_1^j}{\partial \boldsymbol{\sigma}} : (\boldsymbol{\sigma}^{j+1} - \boldsymbol{\sigma}^j) + \frac{\partial f_1^j}{\partial R}(R^{j+1} - R^j) \tag{26}$$

This equation is similar to:

$$\mathrm{d}f_1 = \frac{\partial f_1^j}{\partial \boldsymbol{\sigma}} : \mathrm{d}\boldsymbol{\sigma} + \frac{\partial f_1^j}{\partial R}\mathrm{d}R \tag{27}$$

When the transformation function is positive, it means that transformation takes place and the martensite volume fraction evolves until the transformation function becomes equal to zero. So with $f_1^{j+1} = 0$ the Eq. (27) gives:

$$0 = f_1^j + \frac{\partial f_1^j}{\partial \boldsymbol{\sigma}} : \frac{\partial \boldsymbol{\sigma}}{\partial z}\mathrm{d}z + \frac{\partial f_1^j}{\partial R}\frac{\partial R}{\partial z}\mathrm{d}z \tag{28}$$

The evolution of the martensite volume fraction during forward transformation is then:

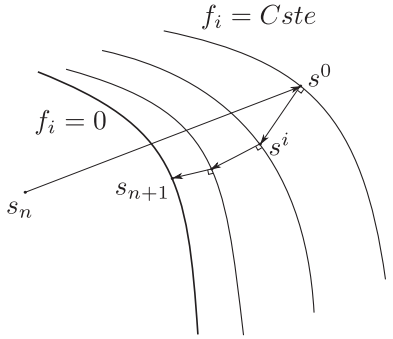

Fig. 22. Schematic evolution of the stress during a step of the numerical integration in the deviatoric plan.

$$\mathrm{d}z = \frac{-f_1^j}{\frac{\partial f_1^j}{\partial \boldsymbol{\sigma}} : \frac{\partial \boldsymbol{\sigma}}{\partial z} + \frac{\partial f_1^j}{\partial R}R'(z)} \tag{29}$$

Where:

$$\frac{\partial f_1^j}{\partial \boldsymbol{\sigma}} = \frac{\partial \overline{\sigma}}{\partial \boldsymbol{\sigma}} + (R(z) + \sigma_0^t(T))\frac{g'(y_\sigma)}{g^2(y_\sigma)}\frac{\partial y_\sigma}{\partial \boldsymbol{\sigma}} \tag{30}$$

$$\frac{\partial \boldsymbol{\sigma}}{\partial z} = \frac{\partial \boldsymbol{\sigma}}{\partial \boldsymbol{\varepsilon}^e}\frac{\partial \boldsymbol{\varepsilon}^e}{\partial \boldsymbol{\varepsilon}^{tr}}\frac{\partial \boldsymbol{\varepsilon}^{tr}}{\partial z} \tag{31}$$

$$\frac{\partial f_1^j}{\partial R} = -\frac{1}{g(y_\sigma)} \tag{32}$$

During reverse transformation the integration procedure is the same as the one used for the forward transformation. The correction procedure concerns the reverse transformation function, f_2, and takes into account the evolution of $\delta(z)$:

$$0 = f_2^j + \frac{\partial f_2^j}{\partial \boldsymbol{\sigma}} : \frac{\partial \boldsymbol{\sigma}}{\partial z}\mathrm{d}z + \frac{\partial f_2^j}{\partial R}\frac{\partial R}{\partial z}\mathrm{d}z + \frac{\partial f_2^j}{\partial \delta}\frac{\partial \delta}{\partial z}\mathrm{d}z \tag{33}$$

The evolution of the martensite volume fraction during reverse transformation is then:

$$\mathrm{d}z = \frac{-f_2^j}{\frac{\partial f_2^j}{\partial \boldsymbol{\sigma}} : \frac{\partial \boldsymbol{\sigma}}{\partial z} + \frac{\partial f_2^j}{\partial R}R'(z) + \frac{\partial f_2^j}{\partial \delta}\delta'(z)} \tag{34}$$

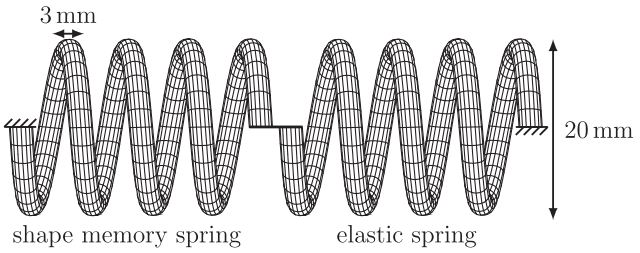

Fig. 23. Mesh of the shape memory-elastic actuator after applying the preload and its dimensions.

where:

$$\frac{\partial f_2^j}{\partial \boldsymbol{\sigma}} = \frac{\partial \bar{\sigma}}{\partial \boldsymbol{\sigma}} + \left(R(z) + \sigma_0^t(T)\right) \frac{g'(y_{\sigma-X})}{g^2(y_{\sigma-X})} \frac{\partial y_{\sigma-X}}{\partial \boldsymbol{\sigma}} \tag{35}$$

$$\frac{\partial f_2^j}{\partial R} = \frac{\partial \overline{\boldsymbol{\sigma} - \boldsymbol{X}}}{\partial (\boldsymbol{\sigma} - \boldsymbol{X})} : \frac{\partial (\boldsymbol{\sigma} - \boldsymbol{X})}{\partial R} - \frac{1}{g(y_{\sigma-X})} + \left(R(z) + \sigma_0^t(T)\right) \frac{g'(y_{\sigma-X})}{g^2(y_{\sigma-X})} \frac{\partial y_{\sigma-X}}{\partial (\boldsymbol{\sigma} - \boldsymbol{X})} : \frac{\partial (\boldsymbol{\sigma} - \boldsymbol{X})}{\partial R} \tag{36}$$

$$\frac{\partial f_2^j}{\partial \delta} = \frac{\partial \overline{\boldsymbol{\sigma} - \boldsymbol{X}}}{\partial (\boldsymbol{\sigma} - \boldsymbol{X})} : \frac{\boldsymbol{\varepsilon}^{tr}}{\sqrt{\frac{3}{2}\boldsymbol{\varepsilon}^{tr} : \boldsymbol{\varepsilon}^{tr}}} + \left(R(z) + \sigma_0^t(T)\right) \frac{g'(y_{\sigma-X})}{g^2(y_{\sigma-X})} \frac{\partial y_{\sigma-X}}{\partial (\boldsymbol{\sigma} - \boldsymbol{X})} : \frac{\boldsymbol{\varepsilon}^{tr}}{\sqrt{\frac{3}{2}\boldsymbol{\varepsilon}^{tr} : \boldsymbol{\varepsilon}^{tr}}} \tag{37}$$

6. Simulation of structures' behavior

After the numerical integration, the model has been implemented in a 3D-finite elements code: Cast3M.

In this part, two mechanisms under cyclic loadings have been considered. Each mechanism is an antagonistic actuator composed of two springs with the same geometrical characteristics. The first actuator is a combination of a shape memory spring and an elastic one with the same elastic properties (see Table 2). The second actuator is the same as the first one, but with a superelastic shape memory spring instead of the elastic one. Those mechanisms were chosen because they are widely used (e.g., Iishi, 2007; Guo et al., 2008; Miga Motor, 2010), have a simple structure and illustrate the behavior under superelastic and stress assisted memory effect loadings.

For each actuator, two steps are considered. The first one is applying a preload which allows us to set up the two springs to obtain a maximal stress level about 430 MPa. The second step consists in the variation of the temperature in order to operate the actuator.

In the following sections, the cyclic thermomechanical behaviors of these two mechanisms are simulated using the developed model for superelasticity and assisted shape memory effect. The material parameters used for the simulations are the ones identified in Table 2.

6.1. Shape memory-elastic antagonistic actuator

The mesh of each spring is composed of 5.760 cubic elements with 20 nodes each, making a total of 26.321 nodes. The Fig. 23 shows the actuator mesh and its characteristics before the preload. The initial pitch of the springs is 4 mm.

The two springs are joined together. During preloading, the left extremity of the actuator is fixed and a fixed displacement is imposed to the right extremity at high temperature. During actuating, four cycles of a thermal loading between 20 °C and 130 °C is applied to the shape memory spring and the elastic spring stays at the room temperature.

Fig. 24a shows the evolution of the actuator displacement during the four thermal cycles. There is only a very small residual displacement due to residual strain in the shape memory spring. So the curves of different cycles appeared as one. Fig. 24b shows the resulting force on the actuator just for the first cycle. During cooling, the forward transformation induced by the thermal variation leads to an elongation of the shape memory spring, which implies a decrease of the stress in the springs. The stress increases back due to the reverse transformation during heating (Fig. 24b).

The Fig. 25a and b show respectively the distribution of the equivalent stress and the martensite volume fraction in the central section of the shape memory spring of the actuator, after cooling. For both, a radial distribution can be observed, which is characteristic of the local torsion induced in a section of a helical spring. But this distribution is not centered in the sections. These results show a transformation level about 25% with a maximal equivalent stress of 225 MPa.

6.2. Shape memory-supererelastic antgonistic actuator

The dimensional characteristics and the mesh of the springs are the same as the previous actuator (Fig. 26). In this case the elastic spring is replaced by a superelastic one.

The limit conditions are similar in the two considered mechanisms. The displacement imposed during the preload phase in this case, is chosen in order to obtain the same level of stress as in the previous mechanism. Since the second spring is superelastic, its

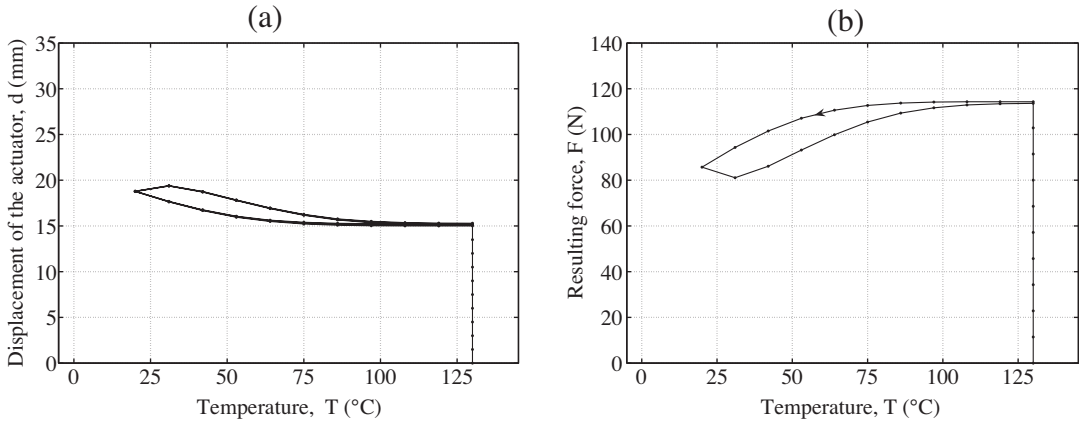

Fig. 24. Evolution of: (a) the actuator displacement versus temperature and (b) the force applied on the actuator versus the temperature.

displacement after applying the preload is larger than the one of the elastic spring in the previous mechanism (Fig. 26).

Fig. 27a shows the evolution of the actuator displacement during the four thermal cycles. In this case, there is a larger residual displacement due to residual strain in the shape memory spring than in the previous mechanism. Fig. 27b shows the resulting force on the actuator just for the first cycle. During cooling, the forward transformation induced by the thermal variation leads to an elongation of the shape memory spring, which implies a decrease of the stress in the springs. The stress increases back due to the reverse transformation during heating (Fig. 27b). The displacement generated by the temperature variation is greater for this actuator than the first one.

The Fig. 28a and b show respectively the distribution of the equivalent stress and the martensite volume fraction in the central section of the shape memory spring of the actuator, after cooling. For both, a radial distribution can be observed, which is characteristic of the local torsion induced in a section of a helical spring. But this distribution is not centered in the sections. These results show a transformation level about 60% with a maximal equivalent stress of 260 MPa.

From the results of the simulation of this two mechanisms involving multiaxial loadings, it appears that the structure effect leads to a heterogeneous state of stress and strain. This leads to low levels of residual strain in comparison with the uniaxial results.

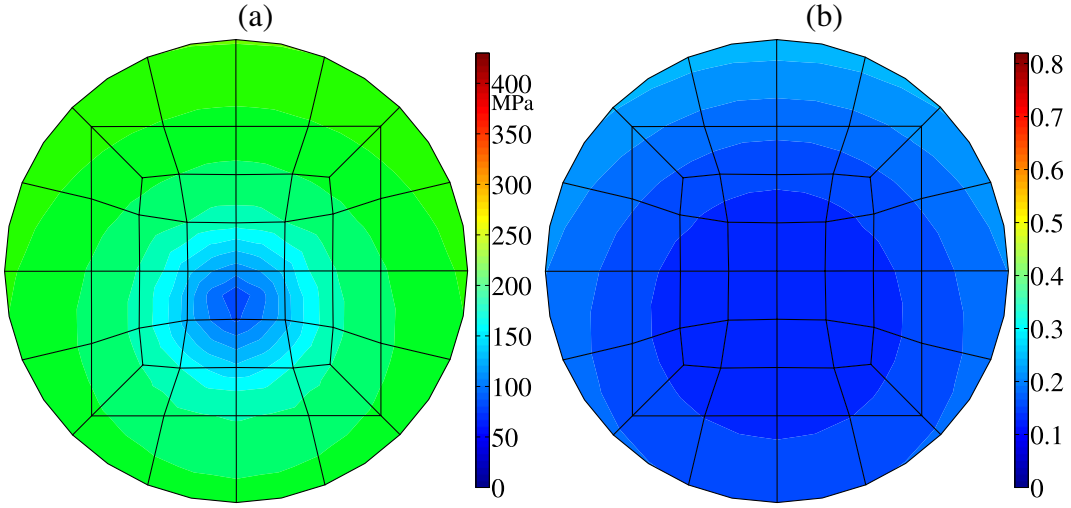

Fig. 25. Distribution of (a) the equivalent stress and (b) the volume fraction of martensite in the central section of the shape memory spring of the actuator after cooling.

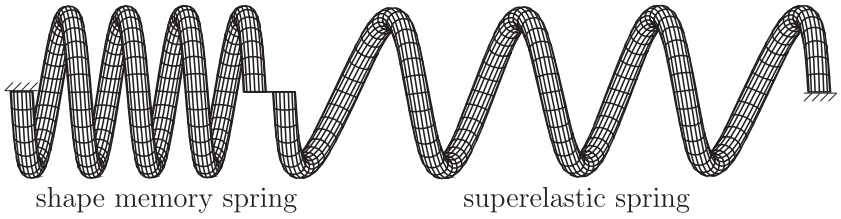

Fig. 26. Mesh of the shape memory-superelastic actuator after applying the preload.

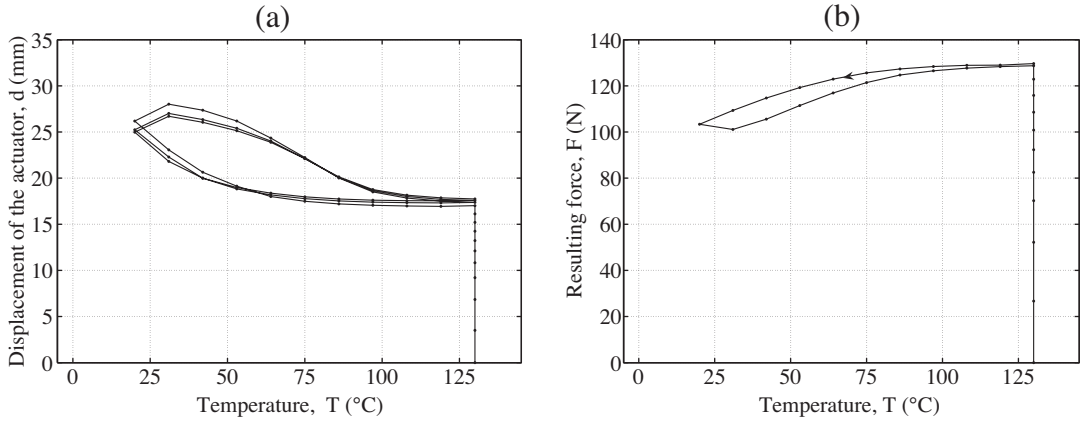

Fig. 27. Evolution of: (a) the actuator displacement versus temperature and (b) the force applied on the second actuator versus the temperature.

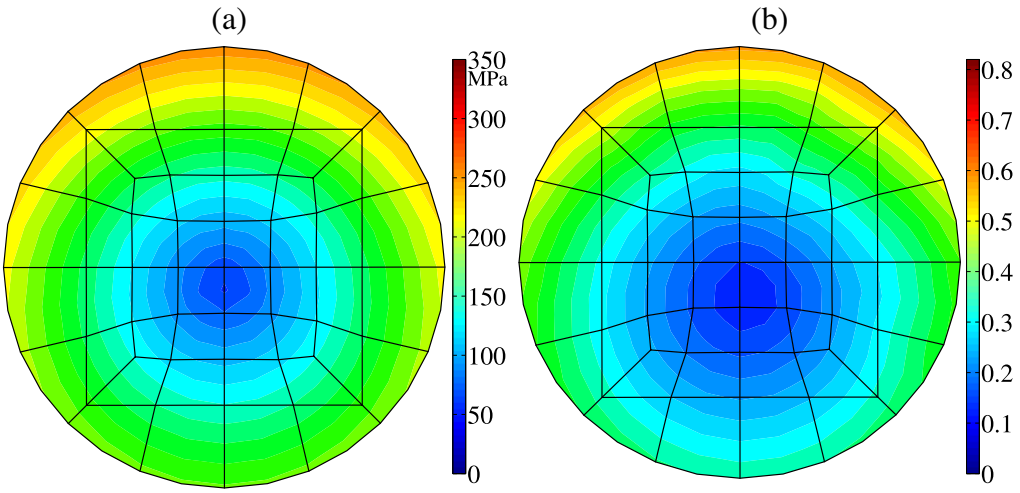

Fig. 28. Distribution of (a) the equivalent stress and (b) the volume fraction of martensite in the central section of the shape memory spring of the second actuator after cooling.

All the results show the good numerical functioning of the proposed model.

7. Conclusion

In this paper, a model permitting the description of the thermomechanical behavior of shape memory alloys under cyclic loadings, has been presented. This model is able to predict the evolution of the residual strain under thermomechanical cyclic loadings by the definition of a jammed martensite volume fraction which evolves with the cumulated transformation strain.

Tensile thermomechanical cyclic loading tests have been performed. These experimental results have permitted the identification and the validation of the model. To validate completely the model, the cyclic complex non-proportional tests will be realised. A particular attention has been paid in the determination of the origin of the residual strain in the studied alloy. It appears that it is mainly due to residual martensite. This allows us to justify the definition of the jammed martensite in the model. Nevertheless, it would be interesting to realise more tests after thermal flash to know if the material recovers its virgin behaviour.

The integration procedure of the model has been detailed. Its particularity is in the handling of the reorientation mechanism, which happens during complex multiaxial loadings.

The model has been implemented in a 3D-finite elements code. The functioning of the two actuators based on a shape memory spring combined with an elastic or a superelastic spring, during thermal cyclic loadings has been simulated. It allows us to compare the two actuators performances with or without the development of a residual displacement.

References

Araya, R., Marivil, M., Mir, C., Moroni, O., Sepulveda, A., 2008. Temperature and grain size effects on the behavior of CuAlBe SMA wires under cyclic loading. Materials Science and Engineering A 496, 209–213.

Arrigoni, M., Auricchio, F., Cacciafesta, V., Petrini, L., Pietrabissa, R., 2001. Mechanical characterisation of orthodontic superelastic Ni-Ti wires. Journal de Physique IV 11, 577–582.

Atanackovic, T., Müller, I., 1995. A new form of the coherency energy in pseudoelasticity. Meccanica 30, 467–474.

Ball, J., James, R., 1987. Fine phase mixtures as minimizers of energy. Archive for Rational Mechanics and Analysis 100, 13–52.

Bigoni, D., Piccolroaz, A., 2004. Yield criteria for quasibrittle and frictional materials. International Journal of Solids and Structures 41 (11–12), 2855–2878.

Bouvet, C., Calloch, S., Lexcellent, C., 2002. Mechanical behavior of a Cu-Al-Be shape memory alloy under multiaxial proportional and nonproportional loadings. Journal of Engineering Materials and Technology 124, 112–124.

Bouvet, C., Calloch, S., Lexcellent, C., 2004. A phenomenological model for pseudoelasticity of shape memory alloys under multiaxial proportional and nonproportional loadings. European Journal of Mechanics – A/Solids 23, 37–61.

Boyd, J.G., Lagoudas, D.C., 1996. A thermodynamical constitutive model for shape memory materials. Part I: the monolithic shape memory alloy. International Journal of Plasticity 12, 805–842.

Falk, F., 1980. Model free energy, mechanics, and thermodynamics of shape memory alloys. Acta Materialia 28, 1773–1780.

Feng, X.Q., Sun, Q.P., 2007. Shakedown analysis of shape memory alloy structures. International Journal of Plasticity 23, 183–206.

Fischer, F.D., Tanaka, K., 1992. A micromechanical model for the kinetics of martensitic transformations. International Journal of Solids and Structures 29, 1723–1728.

Funakubo, H., 1987. Shape Memory Alloys. Gordon and Breach Science Publishers.

Gall, K., Maier, H.J., 2002. Cyclic deformation mechanisms in precipitated NiTi shape memory alloys. Acta Materialia 50, 4643–4657.

Gall, K., Sehitoglu, H., Maier, H.J., 1997. Asymmetric stress–strain response in shape memory alloys. Plasticity '97, Juneau 50, 153–154.

Gedouin, P.A., Arbab Chirani, S., Calloch, S., 2010. Phase proportioning in CuAlBe shape memory alloys during thermomechanical loadings using electric resistance variation. International Journal of Plasticity 26 (2), 258–272.

Guélin, P., 1980. Remarques sur l'hystérésis mécanique. Journal de Mécanique Théorique et Appliquée 19 (2), 217–247.

Guo, S., Sun, X., Iishi, K., Guo, J., 2008. SMA actuator-based novel type of peristaltic micropump. In: International Conference on Information and Automation, pp. 1620–1625.

He, Y.J., Sun, Q.P., 2010. SMA actuator-based novel type of peristaltic micropump. In: International Conference on Information and Automation, pp. 1620–1625.

He, Y.J., Sun, Q.P., Iishi, K., Guo, J., 2010. SMA actuator-based novel type of peristaltic micropump. In: International Conference on Information and Automation, pp. 1620–1625.

Iishi, T., 2007. Combinations and applications of bias method. In: Shape Memory and Superelastic Technologies, pp. 443–446.

Kan, Q., Kang, G., 2010. Constitutive model for uniaxial transformation ratchetting of super-elastic NiTi shape memory alloy at room temperature. International Journal of Plasticity 26, 441–465.

Kang, G., Kan, Q., Qian, L., Liu, Y., 2009. Ratchetting deformation of super-elastic and shape-memory NiTi alloys. Mechanics of Materials 41, 139–153.

Krone, L., Mentz, J., Bram, M., Buchkremer, H.P., Stöver, D., Wagner, M., Eggeler, G., Christ, D., Reese, S., Bogdanski, D., Köller, M., Esenwein, S.A., Muhr, G., Prymak, O., Epple, M., 2005. The potential of powder metallurgy for the fabrication of biomaterials on the basis of nickel-titanium: a case study with a staple showing shape memory behavior. Advanced Engineering Materials 7 (7), 613–619.

Lahoz, R., Puértolas, J.A., 2004. Training and two-way shape memory in niti alloys: influence on thermal parameters. Journal of Alloys and Compounds 381, 130–136.

Lexcellent, C., Leclercq, S., Gabry, B., Bourbon, G., 2000. The two way shape memory effect of shape memory alloys: an experimental study and a phenomenological model. International Journal of Plasticity 16, 1155–1168.

Liu, Y., Xie, Z., Van Humbeeck, J., Delaey, L., 1998. Asymmetry of stress–strain curves under tension and compression for NiTi shape memory alloys. Acta Materialia 46 (12), 4325–4338.

Lu, Z.K., Weng, G.J., 1997. Martensitic transformation and stress–strain relations of shape memory alloys. Journal of the Mechanics and Physics of Solids 45 (11), 1905–1921.

McNaney, J.M., Imbeni, V., Jung, Y., Papadopoulos, P., Ritchie, R.O., 2003. An experimental study of the superelastic effect in a shape-memory Nitinol alloy under biaxial loading. Mechanics of Materials 35, 969–986.

Miga Motor, 2010. http://migamotors.com.

Nemat-Nasser, S., Su, Y., Guo, W.G., Isaacs, J., 2005. Experimental characterization and micromechanical modeling of superelastic response of a porous NiTi shape memory alloy. Journal of the Mechanics and Physics of Solids 53 (10), 2320–2346.

Orgéas, L., Favier, D., 1998. Stress-induced martensitic transformation of a NiTi alloy in isothermal shear, tension and compression. Acta Materialia 46 (15), 5579–5591.

Ortin, J., 1992. Preisach modeling of hysteresis for a pseudoelastic Cu-Zn-Al single crystal. Journal of Applied Physics 71 (3), 1454–1461.

Ortiz, M., Simo, J.C., 1986. An analysis of a new class of integration algorithms for elastoplastic constitutive relations. International Journal for Numerical Methods in Engineering 23 (3), 353–366.

Otsuka, K., Wayman, C.M. (Eds.), 1999. Shape Memory Materials. Cambridge University Press.

Panico, M., Brinson, L.C., 2007. A three-dimensional phenomenological model for martensite reorientation in shape memory alloys. Journal of the Mechanics and Physics of Solids 55, 2491–2511.

Patoor, E., Amrani, M.E., Eberhardt, A., Berveiller, M., 1995. Determination of the origin for the dissymmetry observed between tensile and compression tests on shape memory alloys. Journal de Physique IV 2, 495–500.

Patoor, E., Eberhardt, A., Berveiller, M., 1988. Thermomechanical behavior of shape memory alloys. Archives of Mechanics 40, 755–794.

Raniecki, B., Lexcellent, C., 1994. Rl-models of pseudoelasticity and their specifications for some shape memory alloys. European Journal of Mechanics – A/Solids 13, 21–51.

Saint-Sulpice, L., Arbab Chirani, S., Calloch, S., 2009. A 3D super-elastic model for shape memory alloys taking into account progressive strain under cyclic loadings. Mechanics of Materials 41, 12–26.

Saleeb, A.F., II, S.A.P., Kumar, A., 2010. A multi-axial, multimechanism based constitutive model for the comprehensive representation of the evolutionary response of SMAs under general thermomechanical loading conditions. International Journal of Plasticity. doi: doi:10.1016/j.ijplas.2010.08.012.

Strnadel, B., Ohashi, S., Ohtsuka, H., Ishihara, T., Miyazaki, S., 1995a. Cyclic stress-strain characteristics of Ti-Ni and Ti-Ni-Cu shape memory alloys. Materials Science and Engineering A 202 (1–2), 148–156.

Strnadel, B., Ohashi, S., Ohtsuka, H., Miyazaki, S., Ishihara, T., 1995b. Effect of mechanical cycling on the pseudoelasticity characteristics of Ti-Ni and Ti-Ni-Cu alloys. Materials Science and Engineering A 203 (1–2), 187–196.

Šittner, P., Harra, Y., Tokuda, M., 1995. Experimental study on the thermoelastic martensitic transformation in shape memory alloy polycrystal induced by combined external forces. Metallurgical and Materials Transactions A: Physical Metallurgy and Materials Science 26, 2923–2935.

Sun, Q.P., Hwang, K.C., 1993a. Micromechanics modelling for the constitutive behavior of polycrystalline shape memory alloys – I. Derivation of general relations. Journal of the Mechanics and Physics of Solids 41 (1), 1–17.

Sun, Q.P., Hwang, K.C., 1993b. Micromechanics modelling for the constitutive behavior of polycrystalline shape memory alloys – II. study of the individual phenomena. Journal of the Mechanics and Physics of Solids 41 (1), 19–33.

Taillard, K., 2006. étude du comportement thermomécanique des alliages à mémoire de forme sous sollicitations multiaxiales complexes. Ph.D. thesis, École Normale Supérieure de Cachan.

Taillard, K., Arbab Chirani, S., Calloch, S., Lexcellent, C., 2008. Equivalent transformation strain and its relation with martensite volume fraction for isotropic and anisotropic shape memory alloys. Mechanics of Materials 40 (4–5), 151–170.

Tanaka, K., 1986. A thermomechanical sketch of shape memory effect: one-dimensional tensil behavior. Research Mechanica 18, 251–263.

Tanaka, K., Nishimura, F., Hayashi, T., Tobushi, H., Lexcellent, C., 1995. Phenomenological analysis on subloops and cyclic behavior in shape memory alloys under mechanical and/or thermal loads. Mechanics of Materials 19 (4), 281–292.

Vacher, P., Lexcellent, C., 1991. Study of pseudoelastic behavior of polycrystalline SMA by resistivity measurements and acoustic emission. In: Proceedings of ICM VI, vol. 6, pp. 231–236.

Wang, X., Wang, Y., Lu, Z., Deng, C.H., Yue, Z., 2010. An experimental study of the superelastic behavior in NiTi shape memory alloys under biaxial proportional and non-proportional cyclic loadings. Mechanics of Materials 42, 365–373.

Zaki, W., Zamfir, S., Moumni, Z., 2010. An extension of the ZM model for shape memory alloys accounting for plastic deformation. Mechanics of Materials 42, 266–274.